Chemical Science

ROYAL SOCIETY OF CHEMISTRY

EDGE ARTICLE

View Article Online
View Journal | View Issue

Cite this: *Chem. Sci.*, 2022, **13**, 5155

All publication charges for this article have been paid for by the Royal Society of Chemistry

Received 24th January 2022
Accepted 18th March 2022

DOI: 10.1039/d2sc00459c

rsc.li/chemical-science

A dynamic DNA nanosponge for triggered amplification of gene-photodynamic modulation†

Dan Luo,‡ Xue Lin,‡ Yun Zhao, Jialing Hu, Fengye Mo, Gege Song, Zhiqiao Zou, Fuan Wang and Xiaoqing Liu *

Nucleic acid therapeutics has reached clinical utility through modulating gene expression. As a potential oligonucleotide drug, DNAzyme has RNA-cleaving activity for gene silencing, but faces challenges due to the lack of a safe and effective delivery vehicle and low *in vivo* catalytic activity. Here we describe DNAzyme-mediated gene regulation using dynamic DNA nanomaterials with intrinsic biocompatibility, stability, tumor-targeted delivery and uptake, and self-enhanced efficacy. We assemble programmable DNA nanosponges to package and deliver diverse nucleic acid drugs and therapeutic agents such as aptamer, DNAzyme and its cofactor precursor, and photosensitizer in one pot through the rolling circle amplification reaction, formulating a controllable nanomedicine using encoded instructions. Upon environmental stimuli, DNAzyme activity increases and RNA cleavage accelerates by a supplementary catalytic cofactor. In addition, this approach induces elevated O_2 and $^1O_2$ generation as auxiliary treatment, achieving simultaneously self-enhanced gene-photodynamic cancer therapy. These findings may advance the clinical trial of oligonucleotide drugs as tools for gene modulation.

Introduction

Nucleic acids can be used to modulate gene expression for treating or preventing diseases.[1–4] In very recent years, oligonucleotide therapeutics has received numerous regulatory approvals.[5–7] As an ideal oligonucleotide drug, the RNA-cleaving DNA enzyme (DNAzyme) is a cofactor-dependent DNA that can site-specifically cleave disease genes, and features low-cost synthesis, flexible design, and high specificity.[8–10] Compared with other gene regulation approaches, the cleavage activity of DNAzyme does not require accessory cellular proteins, showing a simple, controllable, and stable catalytic cleavage.[11–13] However, the efficient and safe oligonucleotide delivery and the *in vivo* cleavage activity of DNAzyme remain two major challenges for its applications in clinical trials.

Specifically, due to the low biological stability and non-specific distribution of oligonucleotides under physiological conditions, the inefficient delivery of DNAzyme is an obstacle to clinical applicability.[14,15] To tackle this challenge, various delivery vehicles[16–18] have been explored, mainly viral vectors, liposomes,[19] inorganic nanoparticles,[20,21] and cationic polymers.[22] These delivery approaches protect the nucleic acids from degradation and enhance cellular uptake, yet often suffer from potential cytotoxicity or off-target effects.[23,24] Even some vectors show improved delivery ability; however, due to the insufficient and inefficient cofactor supply in live cells and tissues, the *in vivo* catalytic efficacy of DNAzyme is restricted.[25,26] This results from the fact that the enzymatic activity of DNAzyme is strongly dependent on the level and type of enzyme cofactor, but the DNAzyme delivery systems mostly rely on the intracellular Mg^{2+} ion (0.2–2 mM) as the cofactor, failing to reach an ideal level (5 mM) for high catalytic efficiency.[27] Besides, the Mg^{2+} ion is not usually the most efficient metal ion cofactor that can promote the highest DNAzyme cleavage activity.[28,29] It has been reported that a low level of Mn^{2+} ions (0.2 mM) is sufficient to trigger a complete substrate cleavage, while 15 mM Mg^{2+} ions are needed under the same situation.[30] To overcome this limitation, we and others[30,31] recently demonstrated a cofactor self-sufficient method *via* DNA adsorption onto pre-synthesized particles, yet common to the above gene delivery procedures are the limited cargo loading amount and the requirement of multiple-step and labor-intensive synthesis. As such, the existing DNAzyme carriers and their therapeutics can be inefficient and nonspecific.

Advanced DNA materials show promise to overcome these limitations. Beyond being a genetic material for life, DNA is a building block to create new materials, in particular, assembling or organizing nanomaterials with inherent biocompatibility, complexity and function in a programmable way.[32–34] Particularly, DNA materials can be encoded with versatile functional oligonucleotide sequences, integrated with unique nanoparticles or molecules of interest,[35–37] and endowed with

College of Chemistry and Molecular Sciences, Wuhan University, 430072 Wuhan, P. R. China. E-mail: xiaoqingliu@whu.edu.cn

† Electronic supplementary information (ESI) available: Experimental details; additional characterization and *in vitro* and *in vivo* analysis. See DOI: 10.1039/d2sc00459c

‡ These authors contributed equally to this work.

responsiveness to chemical, biological, and physical cues.[38–41] These aspects make them emerging delivery vehicles for oligonucleotide drugs and therapeutics. We envisage that a new generation of dynamic DNA materials are ready to effectively package and deliver DNAzyme with perfect compatibility, convenience, and precision in a controllable manner; however, there is a lack of exploration. We hypothesize that assembled DNA nanostructures comprising DNAzyme and its cofactor precursor could enhance cleavage activity, and the corresponding therapeutics may be controlled in a programmable manner using encoded instructions in response to signal molecules or stimuli.

Here we present a nucleic acid delivery approach with biomimetic DNA nanoassemblies in a controllable and self-enhanced manner for gene-photodynamic regulation (Scheme 1). This is achieved with DNA drug-encoded and therapeutic-incorporated dynamic nanosponges *via* one-pot synthesis using the rolling circle amplification (RCA) reaction, incorporating aptamer, DNAzyme and its cofactor precursor. Upon DNA-mediated crystallization, the synthetic material is encoded with copious different functional oligonucleotides and intercalated photosensitizers or encapsulated particles. Such a densely packed composition ensures large loading capacity and high biological stability. The multivalent nanosponges with AS1411 aptamers allow specific recognition, delivery, and internalization of the Mn^{2+}-dependent DNAzyme. After tumor targeting by the aptamer, the entrapped MnO_2 reacts with acidic H_2O_2 to generate Mn^{2+} and oxygen in the tumor microenvironment. This self-supplied sufficient and effective DNAzyme cofactors, which is vital for effective silencing of target mRNA in tumor cells. In addition, the stimulus-triggered, self-supplied O_2 enhances photosensitizer-mediated ROS generation for auxiliary photodynamic therapy (PDT). This dynamic DNA material achieves self-enhanced gene silencing and self-amplified photodynamic therapy with high tumor specificity, providing a safe and effective delivery approach for DNAzyme based gene regulation and cancer therapy.

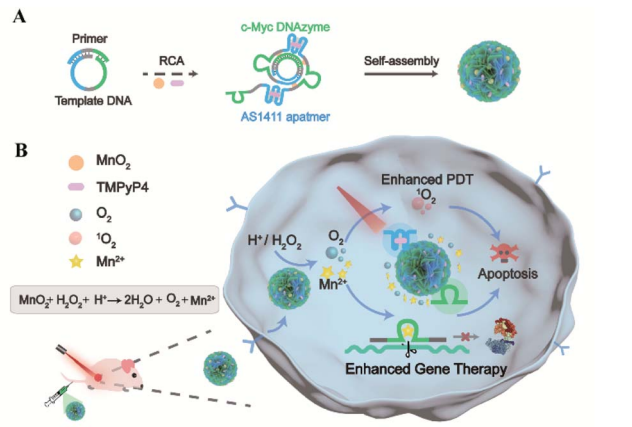

Scheme 1 Illustration of designer dynamic DNA nanosponges for self-boosting gene-photodynamic therapy. (A) Design and assembly of responsive, biomimetic DNA nanosponges *via* one-pot synthesis. (B) Illustration of the dynamic DNA nanostructures for simultaneously enhanced gene-photodynamic therapy by endogenous and exogenous triggers. After tumor targeting by the aptamer, endogenous trigger of the acidic H_2O_2 environment induces the encapsulated MnO_2 to generate Mn^{2+} ions and O_2. The self-supplied metal ions act as effective cofactors of the encoded DNAzyme for the catalytic cleavage of target RNA. Meanwhile, exogenous trigger of light controls the photocytotoxic reactions of the photosensitizers intercalated into DNA, and the resulting singlet oxygen can be further enhanced by the O_2 supplement.

Results and discussion

One-pot synthesis and characterization of dynamic DNA nanosponges by biomimetic crystallization

With a designed template DNA comprising sequences complementary to the AS1411 aptamer and Mn^{2+}-dependent DNAzyme, the RCA reaction proceeded in the presence of the DNAzyme cofactor precursor (MnO_2) and porphyrin photosensitizer (TMPyP4) (Fig. S1†) *via* one-pot synthesis (Scheme 1A and Table S1†). The encoded AS1411 aptamer not only acts as a targeting agent to specifically recognize the nucleolin of cancer cells for precise drug delivery, but also offers the binding site to intercalate the photosensitizer. The encoded DNAzyme is a catalytic oligonucleotide that can specifically recognize and then cleave its substrate sequence in the presence of DNAzyme cofactors. Here c-Myc mRNA, one of the proto-oncogenes identified in many cancers,[42] is used as an example of target gene. A porous DNA nanoassembly can be formed *via* anisotropic nucleic acid-driven crystallization,[43,44] and the DNAzyme cofactor precursor, MnO_2 nanocluster, is spontaneously incorporated into the growing polymer DNA strands and inorganic crystals produced during the RCA process. This enables high loading efficiency and enhanced stability of the respective functional components and drugs, and effective embedding of the enzyme cofactor precursor. Besides, such an approach involves pretty simple and moderate reaction conditions compared to the labor-intensive or postsynthetic modifications related to the preparation of multifunctional DNA nanostructures.[45]

After confirming the successful generation of the circular template and high molecular weight RCA product by native polyacrylamide gel electrophoresis (PAGE) (Fig. 1A), the morphology and size of the particles were investigated by scanning electron microscopy (SEM) and dynamic light scattering (DLS). The SEM image indicated that the DNA nanoassembly incorporating the aptamer, DNAzyme, MnO_2, and photosensitizer (ADMP) was spherical in shape with sponge-like porosities and uniformly sized with a 350 nm diameter (Fig. 1B), which was consistent with the DLS results (Table S2†). Then, we calculated the average replicated copies for each template DNA (Table S3†). The high replication efficiency of the RCA method verifies that the DNA nanosponge delivery vehicles ensure functional nucleic acid cargo delivery. Such a monodisperse and densely packed DNA nanostructure may be the result of the porous structure of the assembly and multiple interactions such as van der Waals forces and inner-sphere coordination between the MnO_2 nanocluster and nucleic acid.[46–48]

MnO_2 provides Mn^{2+} and O_2 upon tumor microenvironment stimuli, which plays an indispensable role in the catalytic

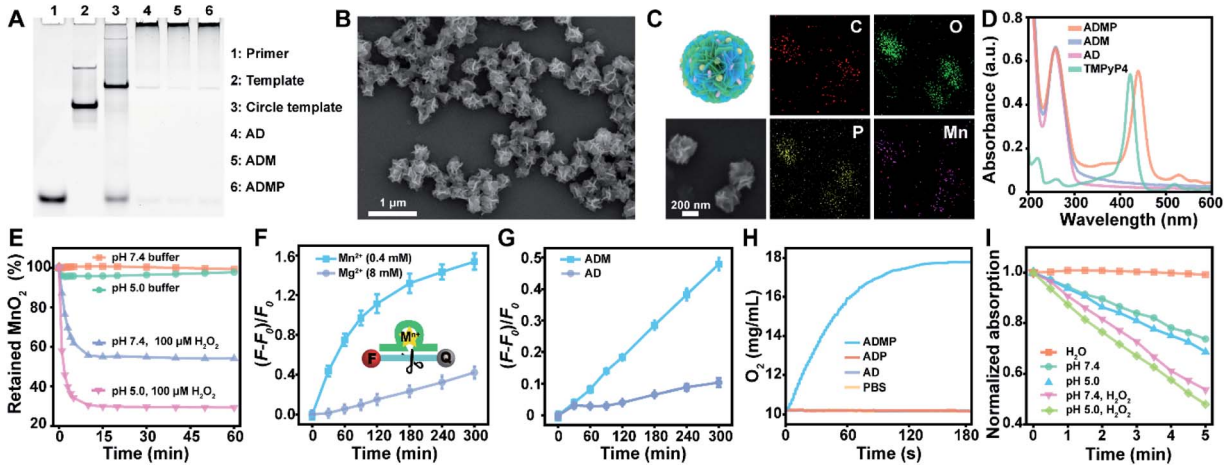

Fig. 1 Synthesis and characterization of DNA nanosponges with a self-supplied enzyme cofactor, enhanced cleavage activity, and supplemental oxygen and singlet oxygen under environmental stimuli. (A) Native PAGE for determining DNA structure. (B and C) SEM image (B) and the corresponding elemental mapping (C) of nanosponge ADMP. (D) UV-vis absorption spectra of AD, ADM, ADMP, and TMPyP4. (E) Acidic H_2O_2-triggered degradation of ADMP. (F) Higher catalytic cleavage activity of AD with Mn^{2+} (0.4 mM) than that with Mg^{2+} (8 mM) as the DNAzyme cofactor. Substrate RNA was labelled with a fluorophore (FAM) and quencher (BHQ1), and the fluorescence was recovered when the substrate was cleaved. (G) Catalytic cleavage activity of AD and ADM in an acidic buffer (pH 5.0) in the presence of H_2O_2. (H) Time-dependent O_2 generation upon separately mixing AD, ADP, and ADPM with H_2O_2 at pH 5.0. (I) Consumption of DPBF over irradiation time due to $^1O_2$ generation by H_2O, ADMP (pH 7.4), ADMP (pH 5.0), ADMP (pH 7.4) plus 100 μM H_2O_2 and ADMP (pH 5.0) plus 100 μM H_2O_2 under 0.2 W cm^{-2} of 660 nm laser irradiation. AD, DNA nanoassemblies with the aptamer and DNAzyme; ADM, DNA nanoassemblies with the aptamer, DNAzyme, and MnO_2; ADP, DNA nanoassemblies with the aptamer, DNAzyme, and photosensitizer; ADMP, DNA nanoassemblies with the aptamer, DNAzyme, MnO_2, and photosensitizer. Data in (F) and (G) are presented as means ± standard deviation (SD) ($n = 3$).

reaction of DNAzyme and therapy enhancement. During the RCA process, the successful incorporation of MnO_2 into the polymer DNA was verified using energy dispersive X-ray spectroscopy (EDX) spectra (Fig. S2†) and the corresponding element mapping (Fig. 1C), indicating the presence of homogeneously scattered carbon (C), oxygen (O), phosphorus (P), and manganese (Mn). Besides, X-ray photoelectron spectra (XPS) illustrated that the split energy of Mn $2p_{3/2}$ and Mn $2p_{1/2}$ was 11.72 eV (Fig. S3A†), which also indicated that the oxidation state of Mn was +4 in ADMP.[49] Simultaneously, the mass ratio between the DNA nanosponge and MnO_2 was calculated to be 1 mg : 47.3 μg by inductively coupled plasma mass spectrometry (ICP-MS) analysis. These results validated that the one-pot synthesized nanocarriers could co-deliver DNAzyme and its cofactor precursor for self-sufficient gene regulation. Besides MnO_2 encapsulation, the successful loading of photosensitizer TMPyP4 in the RCA nanoassemblies was confirmed by UV-vis absorption spectra (Fig. 1D). Compared with the control formulations including DNA nanoassemblies incorporated only with the aptamer and DNAzyme (AD), and DNA nanoassemblies incorporated only with the aptamer, DNAzyme, and MnO_2 (ADM), ADMP showed a classic absorption peak similar to TMPyP4. A high encapsulation efficiency of 91.4% and a drug loading capability of 11.4% (wt/wt) were obtained when 0.1 mM TMPyP4 was used (Table S4†).

As a potential drug vehicle, remaining stable under complex physiological conditions is crucial. The stability of the ADMP was evaluated by incubating them in PBS, DNase I (1 U mL^{-1}), and DMEM (10% serum) for 24 h (Table S5 and Fig. S4†). As revealed by DLS and PAGE, the nanoassemblies exhibited high stability, which is essential for drug delivery and therapy.

Enhanced catalytic activity of DNAzyme through the self-supplied Mn^{2+} cofactor in the presence of signal molecules

To prove the acid/H_2O_2 responsiveness of the nanosponges, the degradation behavior of the encapsulated MnO_2 in DNA nanoassemblies was explored at different pH and H_2O_2. The degradation of MnO_2 could be reflected by the disappearance of its typical absorbance peak at 350 nm (Fig. 1E). Time-dependent absorbance showed that MnO_2 was rather stable under physiological conditions (pH = 7.4); in contrast, MnO_2 decomposed rapidly in acidic buffer (pH = 5.0) with H_2O_2. These data were consistent with the elemental (Mn) analysis by XPS (Fig. S3B†) and ICP-MS (Fig. S5†).

Such reactivity upon acidic H_2O_2 stimuli releases Mn^{2+} ions, which are effective cofactors of DNAzyme for triggering substrate RNA cleavage. The cleavage activity of the DNA nanoassemblies composed of DNAzyme was then investigated by PAGE and fluorescence analysis. We first added exogenous metal ions either Mn^{2+} or Mg^{2+} ions at different concentrations to AD, a DNA nanoassembly incorporated with the aptamer and DNAzyme, in the presence of substrate RNA (Fig. S6, S7† and 1F). Denaturing PAGE analysis indicated that 0.4 mM of Mn^{2+} ions were sufficient to trigger effective substrate cleavage (cleavage efficiency, 85.61%), while 8 mM of Mg^{2+} ions only induced a cleavage efficiency of 55.23% (Fig. S6 and S7†). Similarly, with the extension of cleavage time, the fluorescence intensity of substrate RNA labeled with both a fluorophore and

quencher was significantly increased when 0.4 mM of Mn^{2+} ions were used as the cofactor, while 8 mM of Mg^{2+} resulted in limited fluorescence change (Fig. 1F). These results suggest that Mn^{2+} ions could greatly enhance hydrolysis activity, and promote a dramatically higher DNAzyme activity than Mg^{2+} ions.

To verify the self-enhanced cleavage activity, we designed and took ADM, a DNA nanoassembly incorporated with the aptamer, DNAzyme and MnO_2 nanocluster, as an example (Fig. S8† and 1G). Both denaturing PAGE and fluorescence results demonstrated efficient substrate cleavage by ADM in an acidic H_2O_2-rich medium, and stronger cleavage was obtained with an elevated amount of ADM (Fig. S8†). Comparison of time-dependent fluorescence changes of ADM and AD indicated that the DNA nanoassembly without MnO_2 (AD) had a negligible cleavage capacity, while ADM had a drastic catalytic activity (Fig. 1G). This resulted from the fact that stimuli of acidic H_2O_2 on ADM induce sufficient Mn^{2+} generation, and these self-supplied Mn^{2+} ions act as enzyme cofactors to increase enzymatic activity. All the data indicate that the one-pot synthesized DNA nanosponges have promising potential in self-promoted RNA-cleaving activity.

Elevated $^1O_2$ generation *via* the acidic H_2O_2-triggered O_2 production

As a crucial component, MnO_2 can not only be reduced into Mn^{2+} as an efficient DNAzyme cofactor for gene regulation, but also generate oxygen for alleviating hypoxia and further enhance PDT that requires the interaction of light, a photosensitizer, and molecular oxygen. Correspondingly, O_2 generation under acidic H_2O_2 conditions was investigated using an oxygen electrode (Fig. 1H). As expected, ADMP showed a significant increase in oxygenation. In contrast, AD and the DNA nanoassembly incorporated with the aptamer, DNAzyme, and photosensitizer (ADP) only led to background signals. This clearly evidenced that due to the incorporated MnO_2, ADMP could catalyze H_2O_2 into O_2.

To verify the nanoassembly-mediated photocytotoxic reactions, we evaluated singlet oxygen ($^1O_2$) production by the activated photosensitizer using 2,2,6,6-tetramethylpiperidine (TEMP) and 1,3-diphenylisobenzofuran (DPBF) (Fig. S9, S10† and 1I). Upon laser irradiation, the typical 1 : 1 : 1 triplet signal characteristic was measured by electron spin resonance (ESR) spectroscopy, which indicated that the reactive oxygen species produced by TMPyP4, ADP and ADMP were $^1O_2$.[50] The DPBF could be oxidized by $^1O_2$ which caused a decrease of its characteristic absorbance peak at 410 nm. The maximum absorption of DPBF was decreased to 73.72% within 5 min upon exposing ADMP to light irradiation under neutral conditions (pH = 7.4). Comparatively, the decrease of DPBF absorption accelerated significantly after the addition of H_2O_2, particularly in acidic media (48.01%), indicating an elevated generation of $^1O_2$, which was ascribed to the generation of oxygen under acidic H_2O_2 conditions. Besides, compared with free TMPyP4, ADMP showed improved $^1O_2$ generation efficiency (Fig. S11†). Thus, these results demonstrated that ADMP could be utilized as a multifunctional and simultaneously self-enhanced therapeutic nanoplatform for gene silencing and auxiliary PDT.

Targeted and intensified intracellular gene silencing and ROS generation with self-sufficient therapeutic DNA nanosponges in response to environmental cues

The performance of the dynamic DNA nanomaterials encoded with diverse functionalities and responsiveness was then investigated in live cells (Fig. 2A). Targeted delivery to specific tumor cells is a prerequisite for cancer therapy, and we first tested the cellular uptake capacity of ADMP by flow cytometry and confocal laser scanning microscopy (CLSM). As the encoded AS1411 aptamer in ADMP can specifically recognize the nucleolin of cancer cells, we used 4T1 cells (mouse breast cancer cell line, nucleolin overexpressed) and MCF-10A (human normal breast cell line, low nucleolin expression) as the target and control cells, respectively. Upon incubating 4T1 cells with Cy5-labeled ADMP, the fluorescence intensity of the cells gradually increased and reached a saturation point at 8 h (Fig. 2B and C). Moreover, confocal imaging analysis demonstrated that the fluorescence signal was stronger in cancer cells than in normal cells (Fig. S12†). These results confirmed that the DNA nanoassemblies encoded with the AS1411 aptamer can specifically recognize and target cancer cells, and then achieve selective cellular uptake. To further examine the enhanced uptake mediated by the specific binding between AS1411 and nucleolin, the 4T1 cells were preincubated with an excess amount of free AS1411 for 1 h to block the nucleolin acceptor and then treated with Cy5-labeled ADMP under the same conditions. A noticeably lower fluorescence signal was observed in 4T1 cells than that in an unblocked group under CLSM (Fig. S13†), confirming the reliable cancer cell-specific uptake. Moreover, the intracellular distribution of ADMP was evaluated by incubating 4T1 cells with Cy5-labeled ADMP. After incubation for 6 h, a Pearson's correlation coefficient of 0.78 was calculated from the colocalization of ADMP and lysosomes, which indicated that Cy5-labeled ADMP could be localized in lysosomes after internalization by 4T1 cells (Fig. S14†). As time extended, ADMP could eventually escape from the lysosomes.

Next, we explored the DNAzyme-mediated, cofactor-self-supplied mRNA cleavage and O_2-evolving $^1O_2$ generation upon light illumination in 4T1 cells. Here c-Myc mRNA, a proto-oncogene, was used as an example of target gene to cleave. Down-regulation of c-Myc mRNA could inhibit the progression of a wide range of cancers and has been identified in many different types of cancers such as breast cancer.[42] As demonstrated before, the encapsulated MnO_2 in ADM could be decomposed into Mn^{2+} ions in the tumor microenvironment, which acted as DNAzyme cofactors to improve substrate cleavage efficiency. Correspondingly, we designed control nanoassembly AD (no MnO_2 encapsulated) to verify the role of MnO_2 in ADM for gene silencing. Meanwhile, to examine the RNA-cleaving activity of DNAzyme, we used mutant DNAzyme (mutD) and designed control nanoassemblies AmutD and AmutDM, which had no DNAzyme activity and were unable to cleave the mRNA substrate.

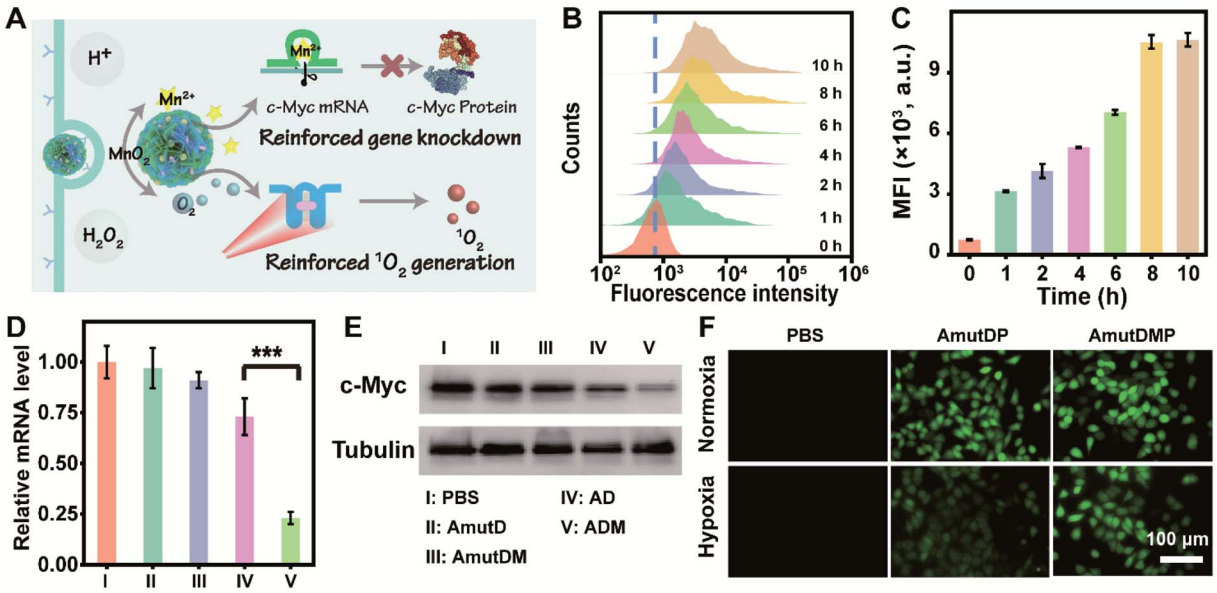

Fig. 2 DNAzyme-mediated enhanced gene silencing and $^1O_2$ generation in cancer cells by the active targeting and responsive DNA nanoassembly. (A) Depiction of cancer-targeted, stimulus-triggered, and self-reinforced gene knockdown and $^1O_2$ generation in live cells. (B and C) Time-dependent internalization of Cy5-labeled AMDP into 4T1 cells determined by flow cytometry. Representative histogram results (B) and quantification of the mean fluorescence intensity (MFI) (C) are shown. (D) qRT-PCR analysis of c-Myc mRNA in 4T1 cells incubated separately with PBS (I), AmutD (II), AmutDM (III), AD (IV), and ADM (V). Results are presented as means ± standard deviation (SD) ($n = 3$). Statistical significance was calculated by one-way ANOVA with Tukey's post hoc test: ***$p < 0.001$. (E) Western blot analysis of c-Myc protein expression of 4T1 cells with different treatments. (F) Detection of $^1O_2$ generation in 4T1 cells by DCFH-DA. The cells were incubated with PBS, AmutDP, and AmutDMP in both normoxia and hypoxia under 660 nm laser irradiation (0.2 W cm^{-2}) for 5 min. AmutD, the DNA nanostructure with the aptamer and mutant DNAzyme; AmutDM, the DNA nanostructure with the aptamer, mutant DNAzyme, and MnO_2; AmutDMP, the DNA nanostructure with the aptamer, mutant DNAzyme, MnO_2, and photosensitizer.

After incubating with different materials, the relative expression of c-Myc mRNA in 4T1 cells was investigated using quantitative real-time polymerase chain reaction (qRT-PCR) assay (Fig. 2D). The mRNA level of c-Myc was successfully inhibited by 77% after the treatment with ADM. As crucial controls, the catalytically inactive AmutD and AmutDM showed negligible influence on the expression of c-Myc mRNA in 4T1 cells, while cofactor deficient AD reduced the mRNA level of c-Myc mRNA by 27%, showing a weaker mRNA-cleavage ability than ADM. Besides, the expression of protein c-Myc was monitored using western blot (Fig. 2E), and the result was consistent with that of the qRT-PCR assay. These data demonstrated strongly that the crystalized DNAzyme/MnO_2 nanosponges could efficiently cleave their target mRNA, as this approach offers a prospective gene regulation that self-supplied effective enzyme cofactors and copious therapeutic DNAzymes.

To explore the feasibility of auxiliary PDT, we further designed a DNA nanoassembly incorporated with the aptamer, mutant DNAzyme and photosensitizer (AmutDP), and a DNA nanoassembly incorporated with the aptamer, mutant DNAzyme, MnO_2, and photosensitizer (AmutDMP) and evaluated the intracellular ROS generation under illumination (Fig. 2F). A ROS probe, 2′,7′-dichlorofluorescein diacetate (DCFH-DA), which could be oxidized by $^1O_2$ and generate a fluorescence indicator DCF, was applied to monitor $^1O_2$ generation in 4T1 cells. It should be noted that under normoxic conditions (21% O_2) the oxygen level is enough for $^1O_2$ production. Therefore, upon 660 nm laser irradiation, both AmutDP- and AmutDMP-treated 4T1 cells displayed bright green fluorescence under normoxia. However, under hypoxic conditions (1% O_2), the cells incubated with AmutDMP showed an evidently stronger fluorescence than those treated with AmutDP, suggesting that the encapsulated MnO_2 in DNA nanosponges self-supplied oxygen *in situ*, and further induced elevated $^1O_2$ generation. Thus, the auxiliary photocytotoxic reaction of the DNA nanosponges could be utilized for enhancing the therapeutic effect.

Simultaneously enhanced and synergistic gene-photodynamic therapy *in vitro*

The enhanced gene silencing and intensified ROS generation in cancer cells using the dynamic materials provided an opportunity for tumor-specific treatment with high efficacy; subsequently, we evaluated the *in vitro* synergistic gene-photodynamic therapy (Fig. 3A). First, cell viability was determined with cell counting kit-8 (CCK-8) assays. In the dark, treating 4T1 cells with different concentrations of AmutDMP caused negligible phototoxicity (Fig. S15†). Besides, when using nucleolin-negative MCF-10A cells as control cells, lower cytotoxicity was obtained after incubating with different DNA materials with or without light exposure (Fig. 3B). These results indicated satisfactory biocompatibility of the nanoparticles.

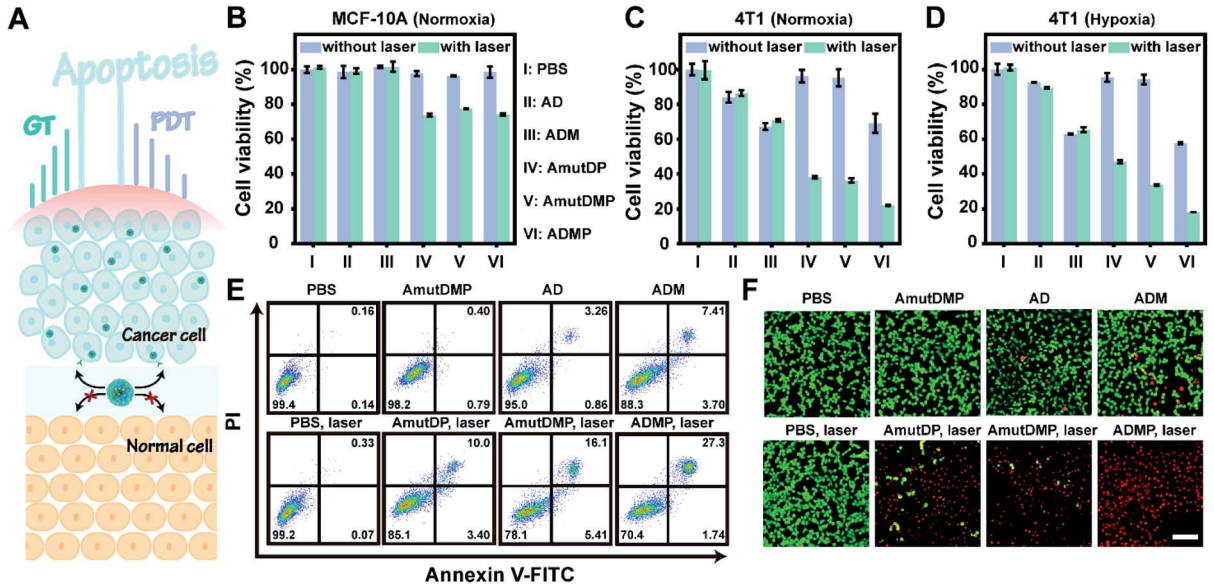

Fig. 3 DNA nanoassemblies induce strong and specific cancer cell apoptosis through simultaneously enhanced gene-photodynamic therapy. (A) A schematic diagram of *in vivo* synergistic cancer-specific therapy. (B–D) Cell viability of MCF-10A (B) and 4T1 cells incubated with PBS (I), AD (II), ADM (III), AmutDP (IV), AmutDMP (V), and ADMP (VI) in normoxia (C) and hypoxia (D) with or without irradiation. Results are presented as means ± standard deviation (SD) ($n = 3$). (E and F) Flow cytometric analysis (E) and live/dead staining (F) of 4T1 cells treated with PBS, AmutDMP, AD, ADM, PBS plus laser, AmutDP plus laser, AmutDMP plus laser, and ADMP plus laser. Laser, 660 nm; power density, 0.2 W cm^{-2}; duration, 5 min. Scale bar, 50 μm.

Then the therapeutic performance of the DNA nanoassemblies was evaluated *in vitro* by comparing the viability of 4T1 cells incubated with different materials with or without irradiation including PBS (I), AD (II), ADM (III), AmutDP (IV), AmutDMP (V), and ADMP (VI) (Fig. 3C and D). Consistent with the results of qRT-PCR and western blot, the cytotoxicity of the AD-treated group was obviously weaker than that of ADM. This is because the MnO_2-encapsulated DNAzyme nanoassemblies could release cofactor Mn^{2+} ions under the tumor microenvironment (acid/H_2O_2 conditions), to enhance gene therapy (GT) effectively. Moreover, when exposed to laser irradiation, the photocytotoxicity of AmutDP and AmutDMP was similar under normoxia; however, the cytotoxicity of AmutDP was obviously lower than that of the latter under hypoxia, demonstrating that the O_2 generated from MnO_2 could relieve tumor hypoxia and enhance PDT efficacy. In addition, among all the materials ADMP with activated gene regulation and the auxiliary photodynamic effect caused the highest cell death after 660 nm photoirradiation. Subsequently, the cytotoxicity of ADMP was further evaluated at various concentrations both in the dark and with light exposure (Fig. S16†). A dose-dependent cytotoxicity was observed in the dark *via* gene regulation, while the viability of 4T1 cells was further decreased once exposed to laser irradiation, suggesting a synergistic gene-photodynamic therapy. Secondly, the *in vitro* therapeutic performance of ADMP was investigated by flow cytometry assay and live/dead cell staining (Fig. 3E and F). Comparisons of the extent of apoptosis in 4T1 cells using different materials and conditions suggested most remarkable cytotoxicity of ADMP treatment. Also, the determined live/dead ratio of tumor cells with different treatments proved a maximum effect by cofactor self-sufficient gene regulation and O_2-supplied photodynamic therapy.

Effective and safe cancer therapy in 4T1 tumor-bearing mice using the self-sufficient DNA nanoassemblies

In 4T1 tumor-bearing BALB/c mice, the *in vivo* antitumor efficacy of DNA nanosponges was explored using seven mice groups ($n = 5$) with different treatments (Fig. 4A). As shown in Fig. 4B, neither PBS (group I) nor AmutDMP (group II) could inhibit tumor growth. However, the mice treated with AD (group III) and ADM (group IV) had a relatively slow tumor growth rate, demonstrating the gene regulation effect. Moreover, the treatments with AmutDP plus laser (group V) and AmutDMP plus laser (group VI) effectively inhibited tumor growth, ascribed to the photodynamic therapy. Furthermore, the superior tumor restraining of ADM (group IV) over AD (group III) well-illustrated the MnO_2-enhanced gene silencing. Meanwhile, when exposed to laser irradiation, an enhanced PDT performance was observed with AmutDMP (group VI) than with AmutDP (group V) under hypoxic conditions, revealing that the oxygen generated from these nanosponges could promote the generation of $^1O_2$. Among all the groups, the mice treated with ADMP under irradiation (group VI) had the maximum antitumor inhibition effect, which was ascribed to the cooperative effort between the DNAzyme cofactor self-sufficient gene regulation and O_2-supplement photodynamic therapy. All the data were in accord with the results of size and weight changes of tumors after treatment (Fig. 4C and D).

Pathological studies further confirmed the therapeutic outcome (Fig. 4E–G). Immunofluorescence (IF) images

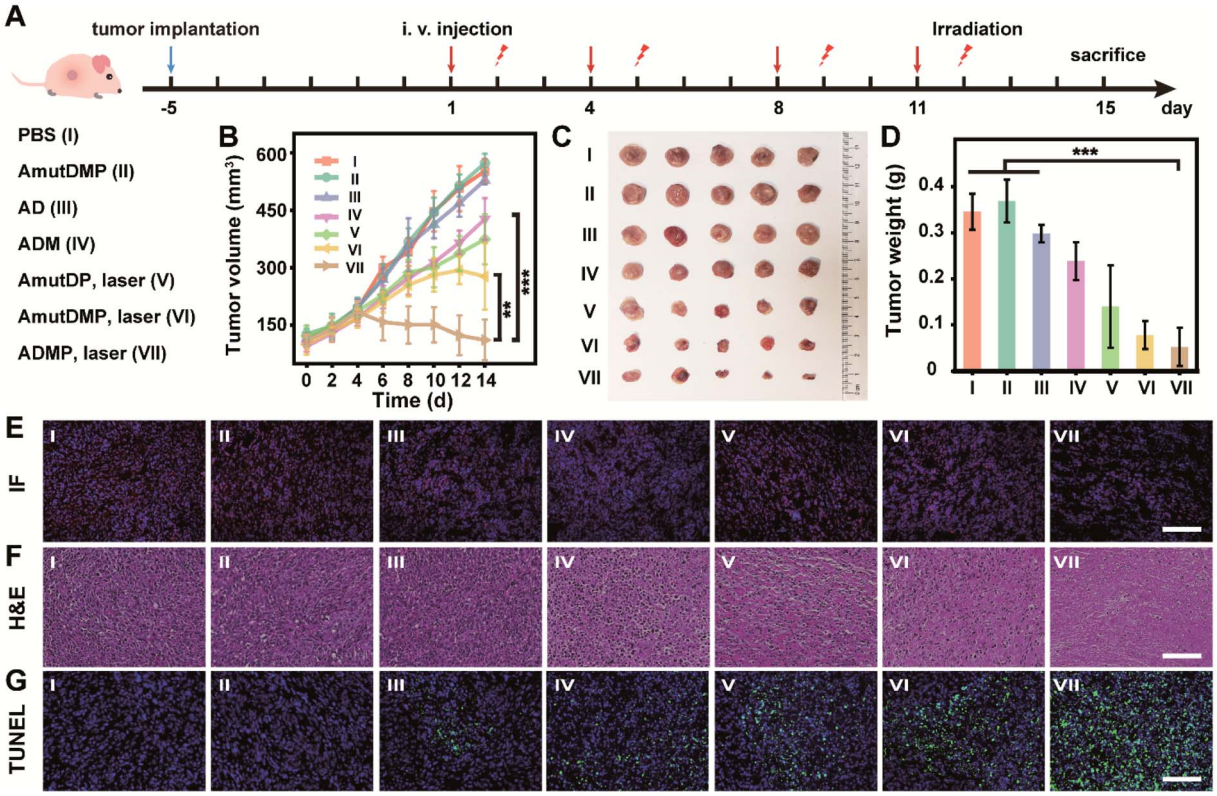

Fig. 4 *In vivo* antitumor efficacy of the therapeutic DNA nanostructures. (A) Scheme of the therapeutic procedure in 4T1 tumor-bearing BALB/c mice. (B) Tumor growth curves. (C and D) Representative tumor picture (C) and weight (D) after different treatments. (E–G) Histological analysis including immunofluorescence (IF) (E), H&E (F), and TUNEL (G) analysis of tumor slices after respective treatment. Each group was injected with 50 μL of the material (corresponds to 3.66 mg kg^{-1} DNA nanoassemblies) and irradiated at 12 h post-injection twice a week. Here the power of photoirradiation (660 nm) was 0.2 W cm^{-2} for 5 min. Scale bar, 100 μm. Error bars represent standard deviations, with $n = 5$ independent replicates. Statistical significance was calculated by one-way ANOVA with Tukey's post hoc test: $^{**}p < 0.01$, $^{***}p < 0.001$.

displayed a weaker red emission of tumor slices treated with ADM (group IV) than those treated with AD (group III) (Fig. 4E), indicating that the MnO_2-encapsulated DNAzyme nanoassemblies could inhibit the expression of c-Myc protein *via* the self-supplied gene regulation. Subsequently, the pathological morphology of tumor tissue was investigated by hematoxylin-eosin (H&E) staining (Fig. 4F). There was a more severe destruction and more disintegrated nuclei in the tumor cells treated with photoirradiated ADMP, but only partial fibrosis was obtained for the ADM or photoirradiated AmutDMP group. These observations indicated that the combinational therapy achieved the best tumor regression efficacy. Similarly, terminal deoxynucleotidyl transferase-mediated dUTP nick-end labeling (TUNEL) staining demonstrated that our therapy (group VII) induced the most drastic level of tumor cell apoptosis (Fig. 4G). Finally, we confirmed the tumor-targeting ability by fluorescence imaging using different materials (Fig. S17†), which was ascribed to the aptamer-mediated targeting and the enhanced permeability and retention (EPR) effects. Furthermore, we evaluated the biosafety of the therapy by long-term body weight monitoring, hemolysis test, H&E staining of major organs, and biochemical index analysis, and observed no systemic toxicity (Fig. S18–S21†). These observations indicated that the therapeutic nanoassemblies possess excellent biocompatibility and may be promising for use in clinical applications.

Conclusions

Overall, RNA-cleaving DNAzyme holds great promise for gene regulation, but its clinical utility is hindered because of the inefficient delivery and limited enzymatic activity *in vivo*. To this end, we have assembled a dynamic DNA nanomaterial as a safe and effective delivery vehicle that can improve catalytic cleavage efficacy and targeting specificity in response to environmental cues. These DNA nanoassemblies can be programmed to package and deliver diverse cargos *via* one-pot synthesis, leading to densely packed Mn^{2+}-dependent DNAzyme and its cofactor precursor for better stability and DNAzyme activity. In addition, the vehicle is encoded with an aptamer and porphyrin photosensitizer as auxiliary molecular therapeutics for specific and effective cancer cell uptake and apoptosis. Upon tumor microenvironment stimuli, the programmable DNA materials not only self-supply the enzyme cofactor but also generate O_2 *in situ*, which leads to targeted and intensified mRNA cleavage and photosensitizer-mediated ROS generation. These data demonstrate a simultaneously self-enhanced gene silencing and self-enhanced adjuvant PDT both *in vitro* and *in vivo*. Our study

provides a safe and targeted delivery of therapeutics for cancer treatment with programmable and dynamic DNA materials. This delivery approach may improve the utility and translation of DNAzyme to regulate disease-related genes. Furthermore, the delivery platform can be programmed to encode different oligonucleotide drugs and cargos of interest for disease prevention and treatment.

Ethical statement

All animal procedures were in accordance with the National Institutes of Health Guide for the Care and Use of Laboratory Animals and approved by the Use Committee of the Animal Experiment Center/Animal Biosafety Level-III Laboratory of Wuhan University (license number: WP20210450).

Data availability

All data supporting this study are included in ESI.†

Author contributions

Conceptualization, X. Liu and D. Luo; investigation, D. Luo, X. Lin and J. Hu; methodology, D. Luo, X. Lin and Y. Zhao; resources, F. Mo, G. Song, Z. Zou and F. Wang; writing – original draft, D. Luo and X. Lin; visualization, D. Luo and Y. Zhao; writing review & editing, X. Liu, D. Luo and X. Lin; project administration, X. Liu; funding acquisition, X. Liu; supervision, X. Liu.

Conflicts of interest

There are no conflicts to declare.

Acknowledgements

This work is supported by the National Natural Science Foundation of China (21874103 and 22074112).

Notes and references

1 J. A. Kulkarni, D. Witzigmann, S. B. Thomson, S. Chen, B. R. Leavitt, P. R. Cullis and R. van der Meel, *Nat. Nanotechnol.*, 2021, **16**, 630–643.
2 C. E. Dunbar, K. A. High, J. Keith Joung, D. B. Kohn, K. Ozawa and M. Sadelain, *Science*, 2018, **359**, eaan4672.
3 K. A. High and M. G. Roncarolo, *N. Engl. J. Med.*, 2019, **381**, 455–464.
4 G. Rancati, J. Moffat, A. Typas and N. Pavelka, *Nat. Rev. Genet.*, 2018, **19**, 34–49.
5 T. C. Roberts, R. Langer and M. J. A. Wood, *Nat. Rev. Drug Discovery*, 2020, **19**, 673–694.
6 J. Zhou and J. Rossi, *Nat. Rev. Drug Discovery*, 2017, **16**, 181–202.
7 H. Ledford, *Nature*, 2018, **560**, 291–292.
8 S. K. Silverman, *Trends Biochem. Sci.*, 2016, **41**, 595–609.
9 A. A. Fokina, D. A. Stetsenko and J.-C. François, *Expert Opin. Biol. Ther.*, 2015, **15**, 689–711.
10 Q. Wang, K. Tan, H. Wang, J. Shang, Y. Wan, X. Liu, X. Weng and F. Wang, *J. Am. Chem. Soc.*, 2021, **143**, 6895–6904.
11 H. K. Karnati, R. S. Yalagala, R. Undi, S. R. Pasupuleti and R. K. Gutti, *Tumor Biol.*, 2014, **35**, 9505–9521.
12 Y. Wang, K. Nguyen, R. C. Spitale and J. C. Chaput, *Nat. Chem.*, 2021, **13**, 319–326.
13 M. Liu, D. Chang and Y. Li, *Acc. Chem. Res.*, 2017, **50**, 2273–2283.
14 J. van Haasteren, J. Li, O. J. Scheideler, N. Murthy and D. V. Schaffer, *Nat. Biotechnol.*, 2020, **38**, 845–855.
15 K. Nguyen, Y. Wang, W. E. England, J. C. Chaput and R. C. Spitale, *J. Am. Chem. Soc.*, 2021, **143**, 4519–4523.
16 I. Lostalé-Seijo and J. Montenegro, *Nat. Rev. Chem.*, 2018, **2**, 258–277.
17 H. Yin, K. J. Kauffman and D. G. Anderson, *Nat. Rev. Drug Discovery*, 2017, **16**, 387–399.
18 M. T. Manzari, Y. Shamay, H. Kiguchi, N. Rosen, M. Scaltriti and D. A. Heller, *Nat. Rev. Mater.*, 2021, **6**, 351–370.
19 J. Buck, P. Grossen, P. R. Cullis, J. Huwyler and D. Witzigmann, *ACS Nano*, 2019, **13**, 3754–3782.
20 H. Wang, Y. Chen, H. Wang, X. Liu, X. Zhou and F. Wang, *Angew. Chem., Int. Ed.*, 2019, **58**, 7380–7384.
21 X. Gong, H. Wang, R. Li, K. Tan, J. Wei, J. Wang, C. Hong, J. Shang, X. Liu, J. Liu and F. Wang, *Nat. Commun.*, 2021, **12**, 3953.
22 W. Shen, R. Wang, Q. Fan, Y. Li and Y. Cheng, *Gene Ther.*, 2020, **27**, 383–391.
23 D. C. Luther, R. Huang, T. Jeon, X. Zhang, Y. W. Lee, H. Nagaraj and V. M. Rotello, *Adv. Drug Delivery Rev.*, 2020, **156**, 188–213.
24 J. Liu, T. Liu, P. Du, L. Zhang and J. Lei, *Angew. Chem., Int. Ed.*, 2019, **58**, 7808–7812.
25 J. Li, C. Zheng, S. Cansiz, C. Wu, J. Xu, C. Cui, Y. Liu, W. Hou, Y. Wang, L. Zhang, I. T. Teng, H. H. Yang and W. Tan, *J. Am. Chem. Soc.*, 2015, **137**, 1412–1415.
26 Y. Jin, Z. Li, H. Liu, S. Chen, F. Wang, L. Wang, N. Li, K. Ge, X. Yang, X.-J. Liang and J. Zhang, *NPG Asia Mater.*, 2017, **9**, e365.
27 M. Cieslak, J. Szymanski, R. W. Adamiak and C. S. Cierniewski, *J. Biol. Chem.*, 2003, **278**, 47987–47996.
28 S. W. Santoro and G. F. Joyce, *Biochemistry*, 1998, **37**, 13330–13342.
29 W. Zhou, R. Saran and J. Liu, *Chem. Rev.*, 2017, **117**, 8272–8325.
30 H. Fan, Z. Zhao, G. Yan, X. Zhang, C. Yang, H. Meng, Z. Chen, H. Liu and W. Tan, *Angew. Chem., Int. Ed.*, 2015, **54**, 4801–4805.
31 X. Gong, R. Li, J. Wang, J. Wei, K. Ma, X. Liu and F. Wang, *Angew. Chem., Int. Ed.*, 2020, **59**, 21648.
32 Q. Hu, H. Li, L. Wang, H. Gu and C. Fan, *Chem. Rev.*, 2019, **119**, 6459–6506.
33 B. R. Madhanagopal, S. Zhang, E. Demirel, H. Wady and A. R. Chandrasekaran, *Trends Biochem. Sci.*, 2018, **43**, 997–1013.
34 A. R. Chandrasekaran, *Nat. Rev. Chem.*, 2021, **5**, 225–239.

35 Y. Gu, M. E. Distler, H. F. Cheng, C. Huang and C. A. Mirkin, *J. Am. Chem. Soc.*, 2021, **143**, 17200–17208.
36 S. Liu, Q. Jiang, X. Zhao, R. Zhao, Y. Wang, Y. Wang, J. Liu, Y. Shang, S. Zhao, T. Wu, Y. Zhang, G. Nie and B. Ding, *Nat. Mater.*, 2021, **20**, 421–430.
37 Z. Wang, L. Song, Q. Liu, R. Tian, Y. Shang, F. Liu, S. Liu, S. Zhao, Z. Han, J. Sun, Q. Jiang and B. Ding, *Angew. Chem., Int. Ed.*, 2021, **60**, 2594.
38 S. Jiang, Z. Ge, S. Mou, H. Yan and C. Fan, *Chem*, 2021, **7**, 1156–1179.
39 J. Gačanin, C. V. Synatschke and T. Weil, *Adv. Funct. Mater.*, 2019, **30**, 1906253.
40 M. Pan, Q. Jiang, J. Sun, Z. Xu, Y. Zhou, L. Zhang and X. Liu, *Angew. Chem., Int. Ed.*, 2020, **59**, 1897–1905.
41 X. Quyang, M. De Stefano, A. Krissanaprasit, A. L. B. Kodal, C. B. Rosen, T. Liu, S. W. Helmig, C. Fan and K. V. Gothelf, *Angew. Chem., Int. Ed.*, 2017, **56**, 14423–14427.
42 S. K. Madden, A. D. de Araujo, M. Gerhardt, D. P. Fairlie and J. M. Mason, *Mol. Cancer*, 2021, **20**, 3.
43 E. Kim, L. Zwi-Dantsis, N. Reznikov, C. S. Hansel, S. Agarwal and M. M. Stevens, *Adv. Mater.*, 2017, **29**, 1701086.
44 E. Kim, S. Agarwal, N. Kim, F. S. Hage, V. Leonardo, A. Gelmi and M. M. Stevens, *ACS Nano*, 2019, **13**, 2888–2900.
45 W. Sun, W. Ji, J. M. Hall, Q. Hu, C. Wang, C. L. Beisel and Z. Gu, *Angew. Chem., Int. Ed.*, 2015, **54**, 12029–12033.
46 Q. Chen, L. Zhang, F. Jiang, B. Wang, T. Lv, Z. Zeng, W. Wu and S. Sun, *Sens. Actuators, B*, 2017, **244**, 1138–1144.
47 L. Wang, Z. Huang, Y. Liu, J. Wu and J. Liu, *Langmuir*, 2018, **34**, 3094–3101.
48 Y. Zhou, L. Zou, G. Li, T. Shi, S. Yu, F. Wang and X. Liu, *Anal. Chem.*, 2021, **93**, 13960–13966.
49 C. Zhang, W.-H. Chen, L.-H. Liu, W.-X. Qiu, W.-Y. Yu and X.-Z. Zhang, *Adv. Funct. Mater.*, 2017, **27**, 1700626.
50 Y. Jin, H. Wang, X. Li, H. Zhu, D. Sun, X. Sun, H. Liu, Z. Zhang, L. Cao, C. Gao, H. Wang, X.-J. Liang, J. Zhang and X. Yang, *ACS Appl. Mater. Interfaces*, 2020, **12**, 26832–26841.